Two-dimensional potassium borides with hidden kagome-like lattice: Topological semimetals, van Hove singularities, and superconductivity

Ting Han,* ShuaiYu Wang,* Bing Han, Yu Liu, Fengyu Li,† and Lei Wang‡
School of Physical Science and Technology, Inner Mongolia University, Hohhot 010021, China

(Received 16 April 2023; revised 18 June 2023; accepted 20 June 2023; published 30 June 2023)

The coexistence of nontrivial topological properties and superconductivity in a material offers the potential to achieve topological superconductivity and Majorana zero modes. However, research on ideal topological semimetals with superconductivity has been limited. In this paper, we utilize first-principles calculations to predict the existence of three two-dimensional potassium borides (K_2B_9, KB_9, and KB_{18}) with a hidden kagome-like lattice structure, inspired by the arrangement of the $K_2B_9^-$ cluster in an inverse sandwich configuration. Our findings reveal that all three materials exhibit phonon-mediated superconductivity, with transition temperatures (T_c) of 12.56, 14.46, and 10.50 K, respectively. Furthermore, K_2B_9 and KB_{18} are identified as topological nodal-line semimetals, while KB_9 demonstrates the characteristics of an ideal Dirac semimetal due to the broken σ_h mirror symmetry and appropriate potassium content. The topological properties arise from the band inversion of the boron atom's $p_x + p_y$ and p_z orbitals within the B_9 layer. Intriguingly, KB_9 exhibits coexisting Dirac points and van Hove singularities near the Fermi level, which are a consequence of the hidden kagome-like lattice, thereby enhancing the superconducting transition temperature (T_c). This research not only sheds light on the pivotal role played by the orbital character of the B_9 layer in the kagome-like lattice of potassium borides but also presents a strategy for achieving the coexistence of topological properties and superconductivity, thereby opening up possibilities for the realization of exotic physics.

DOI: 10.1103/PhysRevB.107.235154

I. INTRODUCTION

With a nontrivial band structure and the associated physical phenomena, topological materials hold great promise for various applications including spintronics, electronics, and quantum computations [1–3]. Among them, topological insulators [1,4,5], topological semimetals [6–12], and topological superconductors [13–21] have emerged as the most significant classes of materials. Remarkably, topological superconductors have garnered particular attention as primary candidates for topological quantum computation, owing to their intriguing and elusive quantum phase characterized by the presence of Majorana zero modes at the boundaries [19–25]. This has spurred a concerted effort towards engineering topological and superconducting quantum states using more commonplace constituents.

One of the key strategies for realizing topological and superconducting quantum states is by inducing superconductivity in topological semimetals [13,26–28]. For example, the topological insulator Bi_2Se_3 can transform into a topological superconductor under high pressure or through doping with external atoms such as Sr, Cu, or Nb [29–31]. Moreover, superconductivity has been observed in the Dirac semimetal Cd_3As_2 [32] as well as in Weyl semimetals including WTe_2 [33], $MoTe_2$ [34], and $TaIrTe_4$ [35]. Furthermore, the potential for superconductivity has been proposed in nodal-line semimetals such as two-dimensional (2D) Cu_2Si [36] and NaAlSi [37]. However, the coexistence of superconductivity with ideal topological semimetals, which host clean Dirac/Weyl fermions near the Fermi energy without the combination of other quasiparticles or bulk states, remains rare, primarily due to the low carrier density near the Fermi level in these materials. Achieving a higher critical temperature (T_c) BCS superconductor necessitates a higher carrier density near the Fermi level [26]. Interestingly, kagome lattices naturally possess van Hove singularities, resulting in a high carrier density. By engineering the kagome lattice in materials, it becomes feasible to realize topological superconducting materials that combine the topological band structure with a high T_c.

The discovery of the well-known superconductor MgB_2 with its unique Dirac-nodal-line structure has sparked interest in exploring metal borides (MBs) for their potential combination of topological properties and superconductivity. So far, superconductivity has been reported in various topological MBs, including Dirac nodal-line semimetals such as $YRuB_2$ and $LuRuB_2$ [38], as well as in AlB_4 [39], AlB_6 [40], and TiB_4 [13]. Nodal net semimetals, including $NbIr_2B_2$ and $TaIr_2B_2$, have also demonstrated superconductivity [41]. Among these materials, the Dirac nodal lines in 2D AlB_6 [40] stand out as its Dirac nodal lines are almost situated precisely at the Fermi level and remain robust even under biaxial strains up to 12%. However, topologically trivial bulk bands also coexist near the Fermi level in AlB_6. Despite its Dirac nodal line near the Fermi level, the bilayer TiB_4 exhibits a relatively low T_c of only 0.82 K [41]. Additionally, although the kagome-lattice compound h-MnB_3 was predicted to have a high T_c of 24.9 K,

*These authors contributed equally to this work.
†fengyuli@imu.edu.cn
‡lwang@imu.edu.cn

its band structure is topologically trivial [42]. Therefore, there is a demand for MBs that possess both an ideal topological band structure and a higher T_c.

In this paper, we employed a crystal structure search method based on first-principles calculations to successfully predict a stable inverse sandwich cluster $K_2B_9^-$. Subsequently, we constructed a 2D K_2B_9 monolayer based on the inverse sandwich structure of $K_2B_9^-$, in combination with previously reported 2D boron planar structures [13,39–41]. Remarkably, our computational results demonstrate that the K_2B_9 monolayer is not only dynamically stable but also exhibits the coexistence of topological nodal-line states and superconductivity, with a critical temperature (T_c) of 12.56 K. To elucidate the mechanism behind superconductivity in the K_2B_9 monolayer, we made the unexpected discovery of three other stable structures: B_9, KB_{18}, and KB_9 monolayers. These structures also exhibit phonon-mediated superconductivity, with T_c values of 1.3 K for B_9, 10.4 K for KB_{18}, and 14.5 K for KB_9. Furthermore, the B_9 and KB_{18} monolayers are nodal-line semimetals, whereas the KB_9 monolayer is an ideal Dirac semimetal. Importantly, we found that the presence of van Hove singularities (vHSs), induced by the kagome-like p_z orbitals of the B_9 layer, is in close proximity to the nodal lines and Dirac points in their respective band structures. This observation plays a critical role in enhancing the superconducting critical temperature. Our theoretical modeling and calculations establish the existence of topological states in the superconducting compounds of the K-B system, thereby enriching the family of topological superconductors among MBs and opening different avenues for exploring exotic physics associated with topological superconductivity.

II. COMPUTATIONAL METHODS

In this study, we initially investigated the stability of the $K_2B_9^-$ cluster. The optimization and frequency calculations of the cluster were performed using the DMOL^3 program [43]. Subsequently, we employed the particle swarm-optimization (PSO) method implemented in the CALYPSO code [44] to search for 2D K_2B_9 structures. Random structures with varying atomic coordinates and lattice parameters were generated to initiate the structure search. The PSO parameters were set with a population size of 30 and a total of 50 generations. The number of K and B atoms per cell was fixed at 2 and 9, respectively. After 30 generations and eliminating irrational structures, we successfully confirmed that our designed K_2B_9 configuration is the global minimum, as documented in Table S1 of the Supplemental Material [45]. The structural optimization, electronic structure, and the related stability properties were performed at the density functional theory (DFT) level using the Vienna *ab initio* simulation package (VASP) [46]. The projector augmented-wave (PAW) method [47] was used to describe electron-ion interactions. The Perdew-Burke-Ernzerhof (PBE) exchange functional [48] in the framework of the general gradient approximation (GGA) was employed for electron-electron exchange correlation. A cutoff energy of 600 eV was utilized for the K-B system. The geometrical optimizations were carried out until the convergence tolerances for energy and atomic forces were below 10^{-5} eV and 0.02 eV/Å, respectively. The Brillouin zone (BZ) sampling was performed using a $7 \times 7 \times 1$ Monkhorst-Pack [49] grid for geometry optimizations and a $13 \times 13 \times 1$ grid for elastic constant calculations. To eliminate interactions between adjacent layers, a 15 Å vacuum was included. The van der Waals (vdW) interactions were accounted for using the Grimme's D2 method [50] to simulate ion adsorption. The phonon spectrum was calculated using the PHONOPY package [51]. Additionally, the thermal stability was assessed through *ab initio* molecular dynamics (AIMD) simulations in a $3 \times 3 \times 1$ supercell at 300 K for 5 ps, employing the Nosé-Hoover method in the NVT [52] ensemble with a time step of 1 fs.

The WANNIER90 package [53] was utilized to construct a tight-binding (TB) model with maximally localized Wannier functions. The WANNIERTOOLS package [54] was employed to determine the edge states using the iterative Green's method. The Z_2 topological invariant was obtained by calculating the parity of wave functions at four time-reversal invariant points, following the method proposed by Xiang *et al.* [55]. The two-dimensional Fermi surface (FS) was calculated using the IFERMI package [56].

The electron-phonon coupling (EPC) and superconductivity calculations were performed using the local density approximation (LDA) as implemented in the QUANTUM ESPRESSO package [57], employing norm-conserving pseudopotentials [58]. A kinetic energy cutoff of 100 Ry and a charge density cutoff of 1000 Ry were chosen for the plane-wave basis. To enhance convergence, a Marzari-Vanderbilt cold smearing method [59] with a width of 0.1 Ry was employed. The structural optimization iterated until the Hellman-Feynman forces on each atom fell below 10^{-5} Ry/bohr. The self-consistent electron density was evaluated using a $14 \times 14 \times 1$ k mesh. Phonon calculations and electron-phonon coupling were performed using a $7 \times 7 \times 1$ q mesh. The EPC was calculated based on the Eliashberg equations, which can be written as [60].

$$\alpha^2F(\omega) = \frac{1}{2\pi N(E_F)} \sum_{qv} \delta(\omega - \omega_{qv}) \frac{\gamma_{qv}}{\hbar\omega_{qv}}, \tag{1}$$

in which ω_{qv} and γ_{qv} are the frequency and linewidth for the phonon mode v at wave vector $\mathbf{q}$, and $N(E_F)$ is the density of states at the Fermi level. The total EPC constant for the investigated compound can be determined by either BZ summation or the frequency-space integration:

$$\lambda = \sum_{qv} \lambda_{qv} = 2 \int \frac{\alpha^2F(\omega)}{\omega} d\omega. \tag{2}$$

Using the McMillian-Allen-Dynes formula, we can evaluate the superconducting transition temperature (T_c) as follows,

$$T_c = \frac{\omega_{\log}}{1.2} \exp\left[\frac{-1.04(1+\lambda)}{\lambda - u^*(1+0.62\lambda)}\right], \tag{3}$$

where u^* is the effective screened Coulomb repulsion constant whose value is generally chosen to be 0.1, and $\omega_{\log}$ is defined through

$$\omega_{\log} = \exp\left[\frac{2}{\lambda} \int \frac{d\omega}{\omega} \alpha^2F(\omega) \log \omega\right]. \tag{4}$$

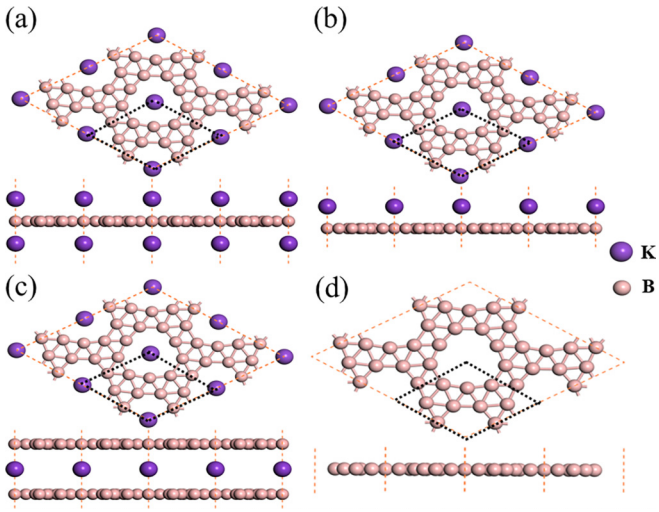

FIG. 1. Lattice structures of (a) K_2B_9 monolayer, (b) KB_9 monolayer, (c) KB_{18} monolayer, and (d) B_9 monolayer.

III. RESULTS AND DISCUSSION

A. Structural models of 2D potassium borides

We first assessed the stability of the $K_2B_9^-$ cluster, which features an inverse sandwich structure (as shown in Fig. S1 in the Supplemental Material [45]). This cluster is a true local minimum as indicated by the absence of any imaginary frequency. The optimized structure of the $K_2B_9^-$ cluster has a point group of D_{9h}, as shown in Fig. S2(a) in the Supplemental Material [45], where K atoms are symmetrically located on both sides of the B_9 ring. The K-B and B-B bond lengths in the $K_2B_9^-$ cluster are 3.43 and 1.56 Å, respectively. The $K_2B_9^-$ cluster also has good thermal stability, because the B_9 ring is well maintained after the 5-ps AIMD simulations at 300 K [see Fig. S2(b) in the Supplemental Material [45]]. Thus, the $K_2B_9^-$ cluster serves as a suitable building block for constructing the 2D K_2B_9 monolayer.

The optimized lattice structure of the assembled K_2B_9 monolayer is depicted in Fig. 1(a), exhibiting a space group of $P\bar{6}2m$ (No. 189) and a lattice constant of $a = b = 5.95$ Å. The K-B bond lengths and the B-B bond lengths within the monolayer fall within the range of 2.96–3.20 and 1.61–1.79 Å, respectively. By varying the ratio of K atoms to the B_9 monolayer, three additional compounds (KB_9, KB_{18}, and B_9) were constructed. The KB_9 (B_9) monolayer is obtained by removing one (two) K atoms from the K_2B_9 monolayer, while the KB_{18} monolayer consists of a K atom sandwiched between two B_9 monolayers. The optimized structures of these compounds are shown in Figs. 1(b)–1(d). Further details regarding their lattice structures can be found in Table S2 in the Supplemental Material [45].

B. The electronic band structure and topology properties

Next, we investigated the electronic properties of the three K-B monolayers. First, we examined the band structure and density of states (DOS) of the KB_{18}, K_nB_9 ($n = 1, 2$) monolayers without considering spin-orbit coupling (SOC), as shown in Figs. 2(a)–2(c). Notably, we observed two crossing points near the Fermi level along the high-symmetry paths Γ-M and K-Γ for the KB_{18} and K_2B_9 monolayers, while the KB_9 monolayer exhibited one crossing point along Γ-M. Additionally, we identified van Hove singularities (vHSs) at the M point in the vicinity of the Fermi level in these band structures. Orbital analyses revealed that these crossing bands and vHSs primarily arise from the B atom orbitals, as indicated by the blue bands. Interestingly, we observed that the K

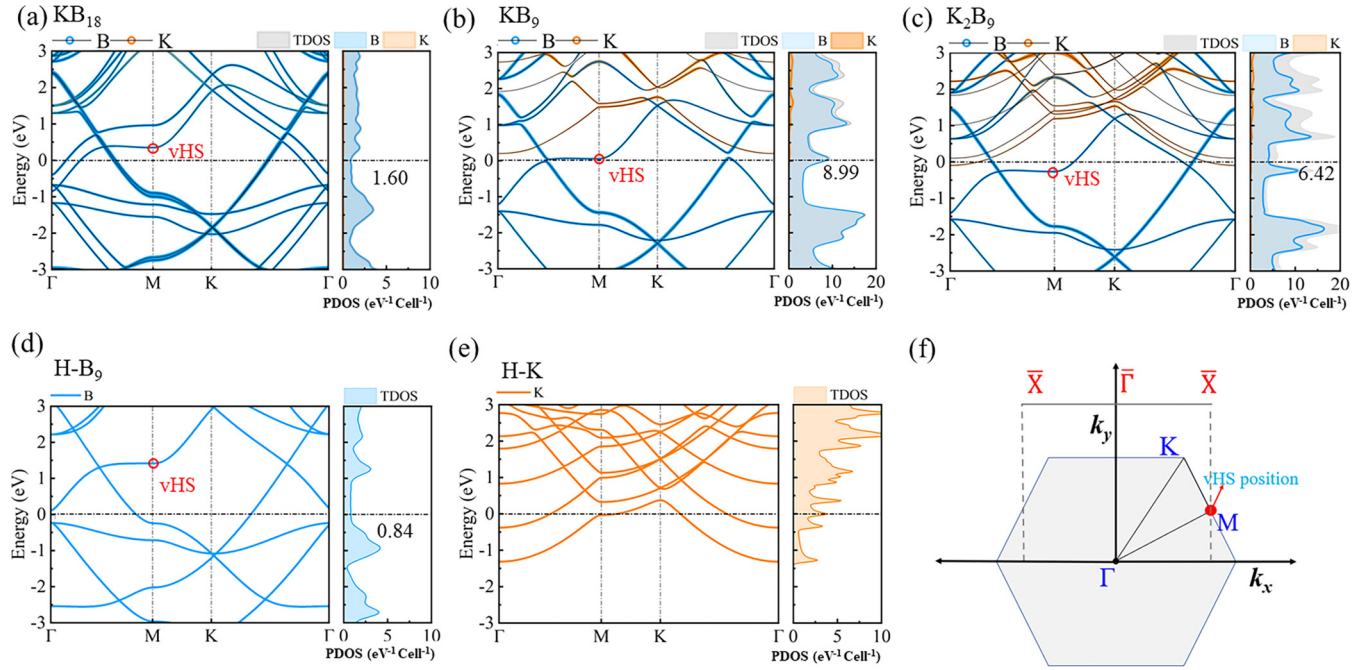

FIG. 2. The orbital-resolved band structures and projected DOS of the (a) KB_{18} monolayer, (b) KB_9 monolayer, (c) K_2B_9 monolayer, (d) B_9 monolayer, and (e) hexagonal K lattice. (f) The 2D BZ and the projected one-dimensional BZ along the (01) direction.

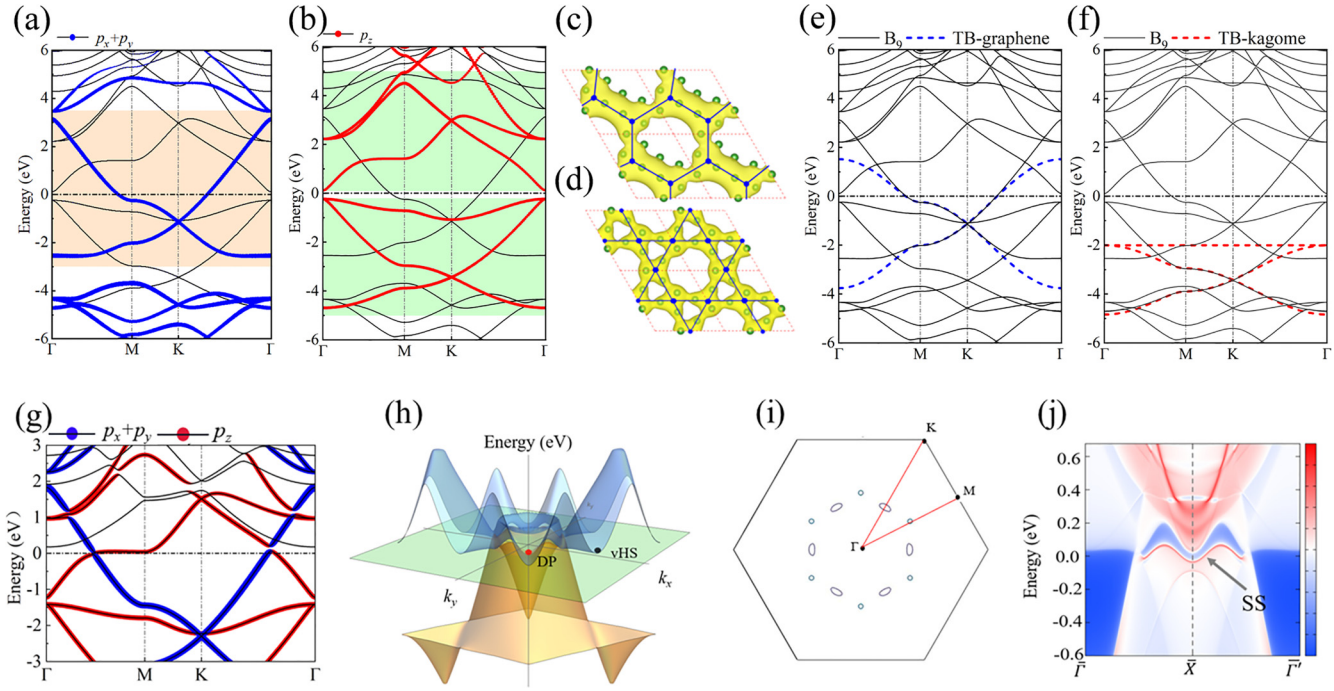

FIG. 3. The band structures of B_9 monolayer with (a) $px + p_y$ orbitals and (b) p_z orbitals. Wave functions at the K point for (c) graphene-like bands and (d) flat bands of kagome-like bands. Comparison of (e) tight-binding graphene-like bands, (f) kagome-like bands, and B_9 bands. (g) Orbital-resolved band structures of the KB_9 monolayer. (h) 3D band structure, (i) 2D Fermi surface, and (j) edge states at the (01) edge of the KB_9 monolayer.

orbitals, represented by the orange bands, shift from energy levels above the Fermi level to energy levels below the Fermi level as we progress from KB_{18} to KB_9 and K_2B_9.

To gain insights into the diverse electronic structures exhibited by these compounds, we analyzed the band structures and DOS of a hexagonal B_9 lattice and hexagonal K lattice, as depicted in Figs. 2(d) and 2(e). Notably, the band structure of the KB_{18}, KB_9, and K_2B_9 monolayers consists of bands originating from the hexagonal K and B_9 monolayers, indicating their heterojunctionlike structures. This observation is consistent with the observed van der Waals (vdW) K-B bond lengths ranging from 2.96 to 3.20 Å. The diverse band structures can be attributed to the charge transfer from the K atom to the B_9 layer. In Table S1 of the Supplemental Material [45], we present the amounts of charge transferred from K to the B_9 layer, which increase with an elevated ratio of K to B_9 layer. This charge transfer effect raises the Fermi level and pushes down the crossing points and vHSs.

Upon analyzing the electronic properties of the B_9 monolayer, we observed the presence of a flat band, Dirac points, and vHSs in the hexagonal B_9 lattice near the Fermi level, as shown in Fig. 2(d). These characteristics align well with the electronic properties of a kagome lattice.

To gain deeper insights into the origins of the flat band, Dirac points, and vHSs in the hexagonal B_9 lattice, we examined the orbital-resolved band structure of the B_9 monolayer, as illustrated in Figs. 3(a) and 3(b) for $p_x + p_y$ and p_z orbitals, respectively. The $p_x + p_y$ orbitals exhibit a band dispersion resembling that of graphene, with the presence of Dirac cones at the K points and saddle points at the M points, as depicted in Fig. 3(a). Additionally, Fig. 3(b) clearly displays two sets of kagome-like bands featuring two Dirac points at the K point and two saddle points at the M point. We further examined the wave function at the K point for the graphene-like bands, as depicted in Fig. 3(c), and the wave function of the flat band for the kagome-like bands, shown in Fig. 3(d). We observed that the spatial distribution of the wave functions supports the characteristic features of graphene-like and kagome-like bands. To model these bands, we constructed tight-binding models based on the graphene lattice and kagome lattice using the Slater-Koster approach [61]. The general Hamiltonian is given by $\hat{H} = \sum_{m\in Z}\sum_{n\in Z}\sum_{l\in Z}\hat{h}m, n, l e^{i\mathbf{k}\cdot\mathbf{R}m,n,l}$, where $\hat{h}_{m,n,l}$ represents the Slater-Koster parameter matrix in different unit cells (see Table S3 in the Supplemental Material [45]). Note that the presence of graphene-like bands and kagome-like bands is further supported by the evolution of the lattice from the typical kagome-B_3 lattice to the B_9 monolayer, as shown in Note S1 and Fig. S4. Moreover, the graphene-like bands and kagome-like bands intersect with each other, forming two crossing points located approximately 1.2 eV above the Fermi level. Importantly, these two crossing points are not isolated but are part of the same nodal loop structure.

To demonstrate the topological properties of the 2D nodal line, we conducted a Z_2 calculation using the method proposed by Xiang *et al.* [55]. This involves calculating the mirror eigenvalues ($\varepsilon_a = +1$ or -1) at four time-reversal invariant points. For the 2D hexagonal lattice, these points consist of Γ $(0.0, 0.0)$, and the three additional points M_0 $(0.5, 0.0)$, M_1 $(0.0, 0.5)$, and M_2 $(0.5, 0.5)$. In a 2D spinless system with time-reversal symmetry, the Z_2 number is defined as $Z_2 = \varepsilon\Gamma\varepsilon_{M_0}\varepsilon_{M_1}\varepsilon_{M_2}$, where $\varepsilon_a = \prod_n^{N_{\rm occ}}\varepsilon_{a_n}$ and $N_{\rm occ}$ represents

TABLE I. The calculated parity eigenvalues and Z_2 of bands near the nodal line.

	Band index	Parity				Z_2
		Γ	M_0	M_1	M_2	
B_9	No. 14	−1	+1	+1	+1	−1
KB_{18}	No. 23	−1	+1	+1	+1	−1
K_2B_9	No. 14	−1	+1	+1	+1	−1

the total number of occupied states. It can be concluded that $Z_2 = [(-1)]^N$, where N is the total number of nodal lines in the 2D system. In the case of the B_9 monolayer, considering the N_{occ} bands, there are three "+" at the M points and one "−" at the Γ point. Therefore, $Z_2 = (+1)^3(-1)^1 = -1$, indicating the nontrivial band topology of the nodal loop surrounding the Γ point in the BZ of the B_9 monolayer, as shown in Table I.

Upon further examination of the band structure of KB_{18}, KB_9, and K_2B_9, we observed that the nodal loop in KB_{18} and K_2B_9 remains intact due to the presence of σ_h mirror symmetry. These structures inherit a Z_2 value of 1 from the B_9 monolayer. However, in the case of the mirror-broken KB_9 monolayer, the nodal loop degrades into Dirac points, as shown in Fig. 3(g). Analyzing the orbital-resolved band structure, we found that the Dirac points mainly arise from the inversion between the $p_x + p_y$ orbitals and the p_z orbitals of the B atoms.

To further explore the topological properties of the KB_9 monolayer, we investigated the Berry phase surrounding the Dirac points. The calculated Berry phase value was found to be π, indicating the nontrivial topological nature of the KB_9 monolayer.

The valence band and conduction band of the KB_9 monolayer exhibit an inverted conelike structure in reciprocal lattice space, as illustrated in Fig. 3(h). This configuration contributes to the formation of two-dimensional Fermi surfaces (FSs) at $k_z = 0$ planes, as depicted in Fig. 3(i). Clear Fermi surfaces are observed along the Γ-M and Γ-K paths.

One of the distinctive features of nontrivial topological materials is the presence of topological edge states. Therefore, we examined the edge states at the (01) edge of the KB_9 monolayer, as shown in Fig. 3(j). The distinct edge states, indicated by the gray arrow, provide further evidence for the topological nature of the KB_9 monolayer.

Notably, the vHSs and Dirac points of the KB_9 monolayer are nearly located at the Fermi level, suggesting the potential coexistence of an ideal topological Dirac cone and high carrier density in this material. This intriguing characteristic opens up different possibilities for the realization of a high-T_c topological superconductor.

C. Electron-phonon coupling and superconductivity

Superconductivity in kagome lattices has been widely recognized [62,63]. Based on the kagome-like band dispersion discussed earlier, we anticipate that the four monolayers mentioned possess similar properties. Therefore, we examine the phonon spectra, phonon densities of states (PhDOS), Eliashberg spectral function $\alpha^2F(\omega)$, and electron-phonon coupling (EPC) $\lambda(\omega)$ of these four monolayers under ambient pressure, as presented in Figs. 4(a)–4(d).

It is evident that the phonon spectra of these four compounds exhibit a striking similarity. The maximum frequency of the phonon spectrum reaches approximately 1400 cm^{-1}, indicating strong valence bonding interactions between the B atoms. This observation aligns well with the valence-band features obtained from the electron localization function (ELF), as illustrated in Fig. S3 in the Supplemental Material [45]. Upon careful comparison, we concluded that the introduction of K atoms leads to the emergence of phonon branches in the frequency range below 200 cm^{-1}. This phenomenon can be attributed to the higher atomic mass of K compared to B, resulting in the domination of the lower-frequency region by the heavier element.

Furthermore, it is noteworthy that the electronic states near the Fermi level arise from both the B and K atoms in K_2B_9, while they originate solely from the B atoms in KB_{18} and KB_9 [refer to Figs. 2(a)–2(d)]. This implies that although the EPC of all three compounds significantly increases at frequencies below 200 cm^{-1}, the primary contribution may not be solely attributed to the K atoms in all cases.

To address this issue, we compiled the phonon spectra of the three compounds weighted by the phonon linewidth γ_{qv} and the ratio of vibration modes between K atoms and B atoms at branch v and wave vector q, as shown in Fig. 5. Evidently the phonon linewidth primarily overlaps with the vibrations of the B atoms, indicating that the B atoms primarily contribute to the EPC at frequencies below 200 cm^{-1} for all three compounds.

Regarding the cumulative EPC, $\lambda(\omega)$, it increases rapidly within this frequency range (see Fig. 4). Furthermore, due to the contribution of the B atoms across the entire frequency range, $\lambda(\omega)$ continues to increase. In contrast to the gradual increase in EPC observed in K_2B_9, KB_{18}, and B_9, the EPC of KB_9 primarily increases at frequencies around 400, 800, and 1300 cm^{-1}. Interestingly, the phonon spectrum of the KB_9 monolayer also exhibits kagome-like bands, and a large phonon linewidth, indicated by the red circle, occurs at the flat band around 1300 cm^{-1} [see Fig. 4(b)], which contributes to the EPC. Moreover, the EPC of these four compounds increases with the increasing DOS at the Fermi level. Among them, KB_9 exhibits the highest EPC value of 1.14, as shown in Fig. 4(b) and Table II, which is significantly influenced by the high DOS induced by the vHSs near the Fermi level.

We further estimated the superconducting transition temperature T_c using the McMillan-Allen-Dynes approach of the Bardeen-Cooper-Schrieffer (BCS) theory, where $T_c = \frac{\omega_{log}}{1.2}\exp[\frac{-1.04(1+\lambda)}{\lambda-\mu^*(1+0.62\lambda)}]$. The results indicate that all four compounds are phonon-mediated superconductors, as summarized in Table II.

With a decrease in the K-to-B_9 ratio, the T_c of the four compounds increases from K_2B_9 (12.56 K) to KB_9 (14.46 K), and then decreases, as shown in Table II and Fig. 6. The increase in T_c from K_2B_9 to KB_9 is attributed to the vHSs in the band structure shifting closer to the Fermi level, resulting in an increase in the DOS at the Fermi level. As the K content decreases from KB_9 to KB_{18} and then to B_9 monolayer, the

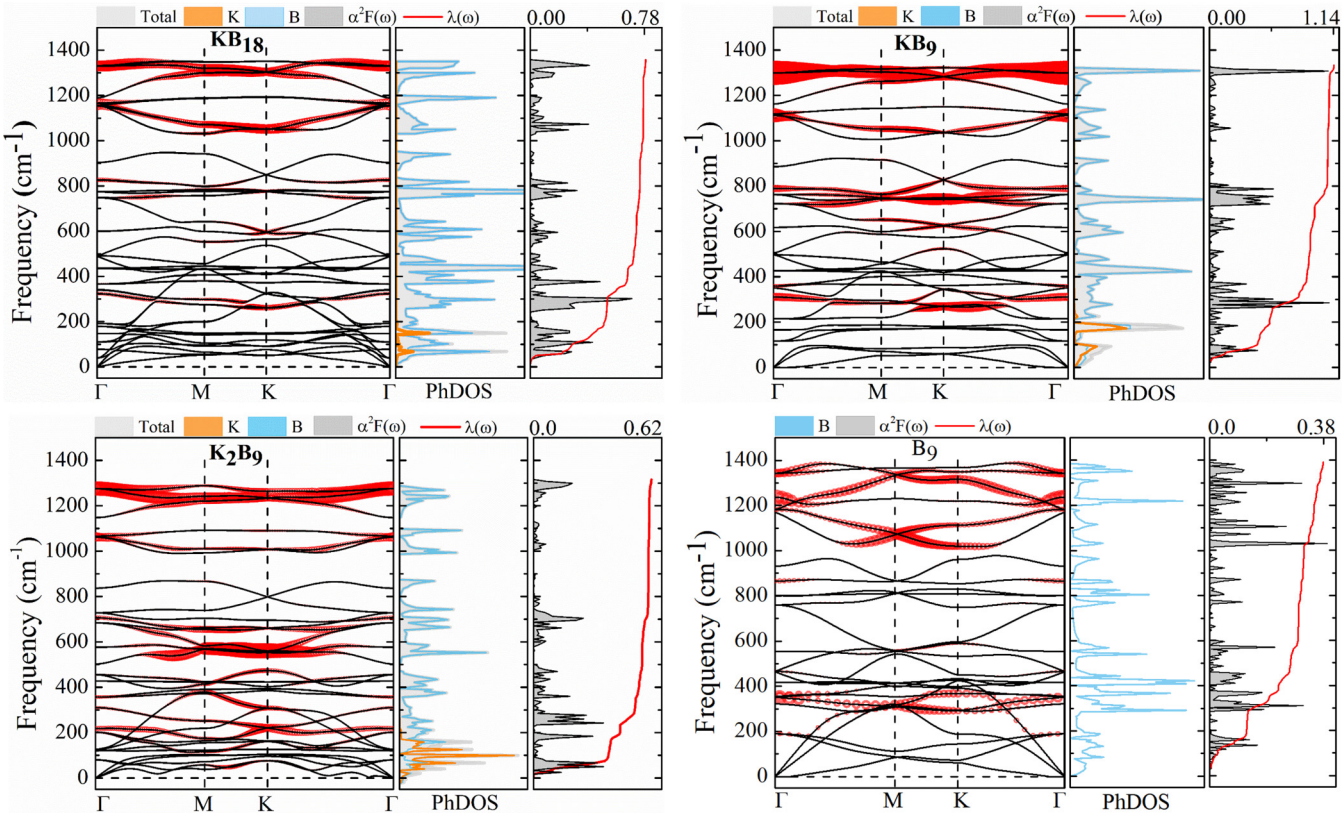

FIG. 4. The phonon dispersion, the phonon DOS (PhDOS) and the Eliashberg function $\alpha^2F(\omega)$, and accumulated EPC constant $\lambda(\omega)$ of (a) KB_{18}, (b) KB_9, (c) K_2B_9, and (d) B_9. Note that the size of red circles in phonon spectrum represents the phonon linewidth γ_{qv}.

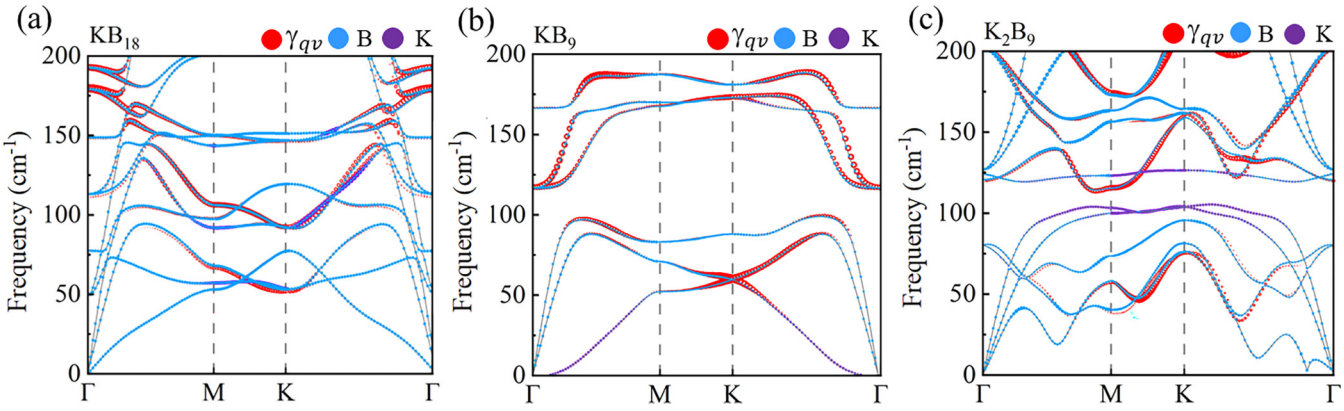

FIG. 5. The phonon linewidth γ_{qv} and the weight of B atoms and K atoms at branch v and wave vector $\mathbf{q}$ of (a) KB_{18}, (b) KB_9, and (c) K_2B_9.

TABLE II. Summary of u^*, λ, $\omega_{\log}$ (in K), T_c (in K), and total DOS at the Fermi level for superconductors with ideal topological bands. (u.c. stands for unit cell.)

Compound	u^*	λ	$\omega_{\log}$ (K)	T_c (K)	$N(E_F)$ (eV^{-1} u.c.$^{-1}$)	Ref.
NaAlSi	/	/	/	7	/	[37]
Au_2Pb	/	/	/	<1.2	/	[64]
Cd_3As_2	/	/	/	2.0	/	[32]
TiB_4	0.1	0.65	57.61	1.66	/	[13]
B_9	0.1	0.36	471.21	0.96	0.84	This paper
KB_{18}	0.1	0.78	240.43	10.5	1.60	This paper
KB_9	0.1	1.14	266.08	14.46	8.99	This paper
K_2B_9	0.1	0.62	137.12	12.56	6.42	This paper

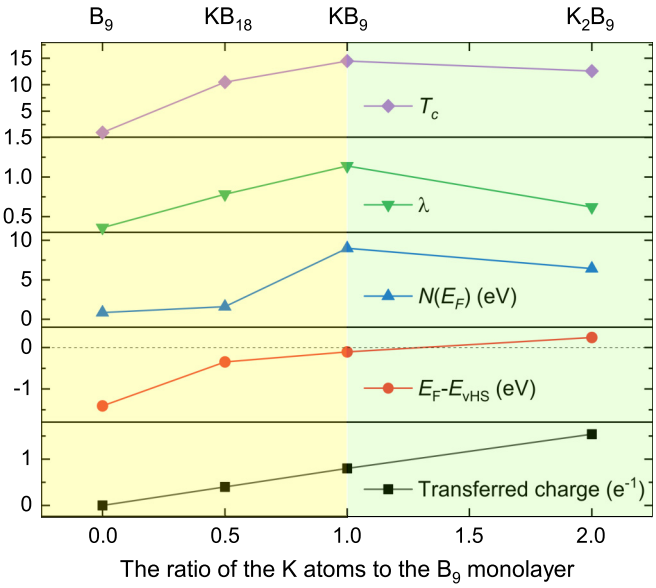

FIG. 6. The curves of transferred charge (from K atoms to B_9 monolayer), density of states at the Fermi level [$N(E_F)$], electron-phonon coupling constant (λ), superconducting transition temperature (T_c), and the difference between the energy of vHSs (E_{vHS}) and the Fermi level (E_F) as a function of the ratio of K atoms to B_9 monolayer.

vHSs gradually move away from the Fermi level, leading to a gradual decrease in the DOS at the Fermi level and a decrease in T_c. In other words, the charge transfer from the K atoms to the B_9 layer and the variation in K content result in different DOS values at the Fermi level for different K-B systems.

Therefore, the reason why KB_9 exhibits the highest T_c among the four compounds is the presence of vHSs near the Fermi level in its band structure and the highest DOS at the Fermi level. This finding is consistent with the previous analysis of the band structure. Additionally, the T_c values of the three K-B compounds are higher than those of NaAlSi, Au_2Pb, and TiB_4 (see Table II).

Furthermore, strain engineering plays a crucial role in the application of 2D materials, allowing for precise control over their electronic properties, EPC strength, and superconducting behavior. Moreover, when considering the practical growth of materials, the influence of external strain arising from substrate interactions becomes a crucial aspect to be addressed. Thus, we investigated the effect of biaxial strains on the EPC and superconductivity of the KB_9 monolayer, the representative of the monolayers studied in this work.

First, we calculated the phonon spectra of the strained KB_9 monolayer for biaxial strains ranging from -1% to 6%. No negative frequencies in the phonon spectra for strains between 0% and 5% were found, indicating the stability of the KB_9 monolayer under tensile strains in this range. Then, we analyzed the superconductivity of the strained KB_9 monolayer. As summarized in Table S4 in the Supplemental Material, the superconducting transition temperature T_c decreases with increasing strain. For example, at a strain of 2%, compared to the strain-free case, the highest phonon frequency is significantly reduced to 1242.74 cm^{-1}. Furthermore, the EPC constant, T_c, and DOS at the Fermi level decrease to 0.68, 13.81 K, and 1.68, respectively, compared to the values of 1.14, 14.56 K, and 8.99 eV^{-1} u.c.$^{-1}$ in the strain-free case. These findings highlight the importance of vHSs in increasing the EPC constant and T_c.

Overall, the analysis of strained KB_9 monolayers indicates that strain engineering can have a significant impact on the superconducting properties of the material, and the presence of vHSs plays a crucial role in enhancing the EPC constant and T_c.

D. Stabilities of the four monolayers

Our above studies revealed that all four monolayers, namely, B_9, K_2B_9, KB_9, and KB_{18}, have excellent topological and superconductivity properties. To ensure the practical applicability of these monolayers, it is crucial to thoroughly examine their stability. Therefore, we carried out the calculations of the cohesive energy, phonon spectrum, elastic constants, and performed AIMD simulations to examine their thermodynamic, dynamic, mechanical, and thermal stability, respectively. By examining these different factors, we can gain a comprehensive understanding of the stability of these structures and evaluate their feasibility for real-world applications.

The cohesive energy (E_{coh}) provides insights into the structural stability of materials, representing the energy gained by arranging atoms in specific crystalline phases or the energy required to break all bonds within the structure. The E_{coh} is calculated using the formula $E_{coh} = (mE_K + nE_B - E_{tot})/(m + n)$, in which E_K and E_B represent the single-atom energies of K and B, respectively, and E_{tot} represents the total energy of the K-B monolayer. According to this expression, higher positive values of E_{coh} indicate greater thermodynamic stability. In our calculations, we obtained $E_K = -0.16$ eV and $E_B = -0.29$ eV. The corresponding E_{coh} values for these structures are provided in Table S5 in the Supplemental Material [45].

The E_{coh} of B_9 (6.01 eV/atom) monolayer is higher than that of the hexagonal-B sheet (5.82 eV/atom), but lower than those of the flat triangular-B sheet (6.58 eV/atom), buckled-triangular B sheet (6.74 eV/atom), and α-B sheet (6.86 eV/atom). The calculated E_{coh} of three K-B compounds are higher than the MgB_4 (4.86 eV/atom), MgB_2 (4.20 eV/atom), and Mg_2B_2 (3.75 eV/atom) (see Table S5 in the Supplemental Material [45]). These results indicate that the B_9 monolayer and three K-B monolayers possess good thermodynamic stability,

No imaginary frequencies were observed in the phonon spectrum over the whole BZ (see Fig. S9 in the Supplemental Material [45]) for all four monolayers, indicating their dynamical stability.

The mechanical stability of these materials was assessed by calculating their elastic constants. The obtained elastic constants are listed in Table S6 in the Supplemental Material [45]. All four compounds satisfy the Born criterion, with $C_{11}C_{22} - C_{12}C_{12} > 0, C_{44} > 0$, indicating their good mechanic stability.

To evaluate their thermal stability, we performed AIMD simulations using $3 \times 3 \times 1$ supercells and performed the simulations for 5 ps at 300 K. The results, presented in Fig. S10 in the Supplemental Material [45], demonstrated that

these four monolayers maintain their initial configurations throughout the simulations, indicating their good thermal stability.

E. Feasibility of experimental realization and proposed synthesis route

The combined use of first-principles calculations, machine learning techniques, and other approaches has accelerated material discovery. In fact, several theoretically predicted materials have been synthesized shortly thereafter. For instance, the planar Cu_2Si monolayer was initially predicted theoretically [67] and later synthesized experimentally [68]. Similarly, the proposal of two-dimensional kagome lattices composed of polymerized heterotriangulene units [69] was followed by the successful fabrication of mesoscale-ordered two-dimensional π-conjugated polymer kagome lattices by Galeotti and collaborators [70].

As for our designed B_9 monolayer, considering the realization of β_{12} and χ_3 boron sheets on an Ag(111) substrate [71], the nice lattice match between the Ag(111) surface and our B_9 monolayer [the lattice length of a 2×2 supercell of the Ag(111) slab is 5.78 Å, quite close to the lattice parameter of 5.79 Å of our B_9 monolayer], as well as the close cohesive energies (β_{12}: 6.06 eV/atom; χ_3: 6.05 eV/atom; our B_9 monolayer: 6.01 eV/atom, at the same level of theory), we conjecture that our B_9 monolayer has a high possibility to be synthesized on an Ag(111) substrate.

On the other hand, it is worth noting that thin films of disordered hexaborides, such as CaB_6 and SrB_6, have been successfully deposited on MgO or Al_2O_3 substrates using the pulsed-laser method [72]. Additionally, we observe a good lattice parameter match between the 2×2 supercell of the MgO(111) slab (5.96 Å) and our K_2B_9 monolayer (5.95 Å). Combined with the confirmation of the global minimum of our K_2B_9 monolayer in the 2D space through the CALYPSO code, our K_2B_9 monolayer exhibits great potential for realization on the MgO(111) substrate using the pulsed-laser method.

IV. CONCLUSIONS

In summary, this study presents the design of K_2B_9, KB_9, and KB_{18} monolayers with a kagome-like lattice structure, achieved through a combination of cluster assembly and first-principles calculations. These monolayers exhibit remarkable stability in terms of their thermodynamic, dynamic, mechanical, and thermal aspects. Extensive first-principles calculations were conducted to investigate their electronic properties, lattice dynamics, electron-phonon coupling (EPC) constants, and superconductivity. Our computations revealed that all three monolayers exhibit phonon-mediated superconductivity. Notably, increasing the ratio of K atoms to the B_9 monolayer brings the van Hove singularities (vHSs) closer to the Fermi level, leading to an enhanced density of states at the Fermi level and an increase in the superconducting transition temperature (T_c). Furthermore, these monolayers possess topological semimetal behavior, with the KB_9 monolayer exhibiting ideal Dirac semimetal characteristics, including Dirac points near the Fermi level. Importantly, the KB_9 monolayer also emerges as the highest-T_c superconductor, with a T_c value of 14.46 K.

Overall, this work presents a promising avenue for the design of high-T_c topological superconductors featuring ideal topological bands. The combination of kagome-like lattice structures, phonon-mediated superconductivity, and topological semimetal properties opens up different possibilities for exploring exotic electronic and superconducting phenomena in two-dimensional materials.

ACKNOWLEDGMENTS

This work was financially supported by the National Natural Science Foundation of China (Grant No. 11964024), the Science Foundation for Youths of Inner Mongolia autonomous region (Grant No. 2023QN01003), the "Grassland Talents" project of the Inner Mongolia autonomous region (Grant No. 12000-12102613), the Startup Project of Inner Mongolia University (Grant No. 21200-5223733), and the young science and technology talents cultivation project of Inner Mongolia University (Grant No. 21200-5223708). The authors are thankful for the computational source provided by Beijing PARATERA and Shanghai Supercomputer Center.

[1] M. Z. Hasan and C. L. Kane, Rev. Mod. Phys. **82**, 3045 (2010).
[2] X.-L. Qi and S.-C. Zhang, Rev. Mod. Phys. **83**, 1057 (2011).
[3] A. Bansil, H. Lin, and T. Das, Rev. Mod. Phys. **88**, 021004 (2016).
[4] J. E. Moore, Nature (London) **464**, 194 (2010).
[5] H. Zhang, C.-X. Liu, X.-L. Qi, X. Dai, Z. Fang, and S.-C. Zhang, Nat. Phys. **5**, 438 (2009).
[6] A. Burkov, Nat. Mater. **15**, 1145 (2016).
[7] H. Weng, X. Dai, and Z. Fang, J. Phys.: Condens. Matter **28**, 303001 (2016).
[8] A. Bernevig, H. Weng, Z. Fang, and X. Dai, J. Phys. Soc. Jpn. **87**, 041001 (2018).
[9] C. Fang, M. J. Gilbert, X. Dai, and B. A. Bernevig, Phys. Rev. Lett. **108**, 266802 (2012).
[10] C.-K. Chiu and A. P. Schnyder, Phys. Rev. B **90**, 205136 (2014).
[11] C. M. Wang, H.-P. Sun, H.-Z. Lu, and X. C. Xie, Phys. Rev. Lett. **119**, 136806 (2017).
[12] B.-J. Yang, T. A. Bojesen, T. Morimoto, and A. Furusaki, Phys. Rev. B **95**, 075135 (2017).
[13] L. Wang, M. Liu, J. Li, R. Li, H. Ma, and X.-Q. Chen, Phys. Rev. B **104**, 195123 (2021).
[14] M. Sato and Y. Ando, Rep. Prog. Phys. **80**, 076501 (2017).

[15] B. A. Bernevig, in *Topological Insulators and Topological Superconductors* (Princeton University Press, Princeton, NJ, 2013).

[16] P. Zhang, K. Yaji, T. Hashimoto, Y. Ota, T. Kondo, K. Okazaki, Z. Wang, J. Wen, G. D. Gu, H. Ding *et al.*, Science **360**, 182 (2018).

[17] S.-L. Yu and J.-X. Li, Phys. Rev. B **85**, 144402 (2012).

[18] G. Xu, B. Lian, P. Tang, X.-L. Qi, and S.-C. Zhang, Phys. Rev. Lett. **117**, 047001 (2016).

[19] W. Liu, L. Cao, S. Zhu, L. Kong, G. Wang, M. Papaj, P. Zhang, Y.-B. Liu, H. Chen, G. Li *et al.*, Nat. Commun. **11**, 5688 (2020).

[20] L. Kong, L. Cao, S. Zhu, M. Papaj, G. Dai, G. Li, P. Fan, W. Liu, F. Yang, X. Wang *et al.*, Nat. Commun. **12**, 4146 (2021).

[21] R. M. Lutchyn, E. P. Bakkers, L. P. Kouwenhoven, P. Krogstrup, C. M. Marcus, and Y. Oreg, Nat. Rev. Mater. **3**, 52 (2018).

[22] Y. Yuan, J. Pan, X. Wang, Y. Fang, C. Song, L. Wang, K. He, X. Ma, H. Zhang, F. Huang *et al.*, Nat. Phys. **15**, 1046 (2019).

[23] S. D. Sarma, M. Freedman, and C. Nayak, npj Quantum Inf. **1**, 15001 (2015).

[24] S. M. Albrecht, A. P. Higginbotham, M. Madsen, F. Kuemmeth, T. S. Jespersen, J. Nygård, P. Krogstrup, and C. Marcus, Nature (London) **531**, 206 (2016).

[25] B. Jäck, Y. Xie, J. Li, S. Jeon, B. A. Bernevig, and A. Yazdani, Science **364**, 1255 (2019).

[26] J. Wang, Natl. Sci. Rev. **6**, 199 (2019).

[27] N. P. Butch, P. Syers, K. Kirshenbaum, A. P. Hope, and J. Paglione, Phys. Rev. B **84**, 220504(R) (2011).

[28] K. Iwaya, Y. Kohsaka, K. Okawa, T. Machida, M. Bahramy, T. Hanaguri, and T. Sasagawa, Nat. Commun. **8**, 976 (2017).

[29] Z. Liu, X. Yao, J. Shao, M. Zuo, L. Pi, S. Tan, C. Zhang, and Y. Zhang, J. Am. Chem. Soc. **137**, 10512 (2015).

[30] S. Yonezawa, K. Tajiri, S. Nakata, Y. Nagai, Z. Wang, K. Segawa, Y. Ando, and Y. Maeno, Nat. Phys. **13**, 123 (2017).

[31] J. Shen, W.-Y. He, N. F. Q. Yuan, Z. Huang, C.-w. Cho, S. H. Lee, Y. S. Hor, K. T. Law, and R. Lortz, npj Quantum Mater. **2**, 59 (2017).

[32] L. He, Y. Jia, S. Zhang, X. Hong, C. Jin, and S. Li, npj Quantum Mater. **1**, 16014 (2016).

[33] P. Li, Y. Wen, X. He, Q. Zhang, C. Xia, Z.-M. Yu, S. A. Yang, Z. Zhu, H. N. Alshareef, and X.-X. Zhang, Nat. Commun. **8**, 2150 (2017).

[34] Y. Qi, P. G. Naumov, M. N. Ali, C. R. Rajamathi, W. Schnelle, O. Barkalov, M. Hanfland, S.-C. Wu, C. Shekhar, Y. Sun *et al.*, Nat. Commun. **7**, 11038 (2016).

[35] K. Koepernik, D. Kasinathan, D. V. Efremov, S. Khim, S. Borisenko, B. Büchner, and J. van den Brink, Phys. Rev. B **93**, 201101(R) (2016).

[36] L. Yan, P.-F. Liu, T. Bo, J. Zhang, M.-H. Tang, Y.-G. Xiao, and B.-T. Wang, J. Mater. Chem. C **7**, 10926 (2019).

[37] S. Uji, T. Konoike, Y. Hattori, T. Terashima, T. Oguchi, T. Yamada, D. Hirai and Z. Hiroi, Phys. Rev. B **105**, 235103 (2022).

[38] Y. Kishimoto, Y. Kawasaki, M. Tanabe, T. Tanaka, T. Ohno, G. Ghosh, A. Tyagi, and L. Gupta, J. Magn. Magn. Mater. **310**, 581 (2007).

[39] S. Abedi, E. T. Sisakht, S. J. Hashemifar, N. G. Cherati, I. A. Sarsari, and F. M. Peeters, Nanoscale **14**, 11270 (2022).

[40] B. Song, Y. Zhou, H.-M. Yang, J.-H. Liao, L.-M. Yang, X.-B. Yang, and E. Ganz, J. Am. Chem. Soc. **141**, 3630 (2019).

[41] Y. Gao, J.-F. Zhang, S. A. Yang, K. Liu, and Z.-Y. Lu, Phys. Rev. B **103**, 125154 (2021).

[42] Z. Qu, F. Han, T. Yu, M. Xu, Y. Li, and G. Yang, Phys. Rev. B **102**, 075431 (2020).

[43] B. Delley, J. Chem. Phys. **113**, 7756 (2000).

[44] Y. Wang, J. Lv, L. Zhu, and Y. Ma, Comput. Phys. Commun. **183**, 2063 (2012).

[45] See Supplemental Material at http://link.aps.org/supplemental/10.1103/PhysRevB.107.235154 for the frequency spectra and atomic configurations of the $K_2B_9^-$ cluster, the electron localization function (ELF) for the K_2B_9, KB_9, KB_{18}, and B_9 monolayers, the phonon dispersion relationships of the KB_9 monolayer with strain from –1% to 6%, the phonon dispersion, PhDOS, and Eliashberg function $\alpha^2F(\omega)$ with accumulated EPC constant $\lambda(\omega)$ of the KB_9 after the tensile strains, the calculated phonon spectra and AIMD simulations of the KB_{18}, KB_9, K_2B_9, and B_9 monolayers, the structure information of the KB_{18}, KB_9, K_2B_9, and B_9 monolayers, and the Slater-Koster parameters for tight-binding graphene-like and kagome-like lattices in different unit cells, which includes Refs. [65,66].

[46] G. Kresse and J. Furthmüller, Phys. Rev. B **54**, 11169 (1996).

[47] P. A. Korzhavyi, I. A. Abrikosov, B. Johansson, A. V. Ruban, and H. L. Skriver, Phys. Rev. B **59**, 11693 (1999).

[48] J. P. Perdew, K. Burke, and M. Ernzerhof, Phys. Rev. Lett. **77**, 3865 (1996).

[49] H. J. Monkhorst and J. D. Pack, Phys. Rev. B **13**, 5188 (1976).

[50] T. Bučko, J. Hafner, S. Lebegue, and J. G. Angyan, J. Phys. Chem. A **114**, 11814 (2010).

[51] A. Togo and I. Tanaka, Scr. Mater. **108**, 1 (2015).

[52] G. Bussi, D. Donadio, and M. Parrinello, J. Chem. Phys. **126**, 014101 (2007).

[53] A. A. Mostofi, J. R. Yates, Y.-S. Lee, I. Souza, D. Vanderbilt, and N. Marzari, Comput. Phys. Commun. **178**, 685 (2008).

[54] Q. Wu, S. Zhang, H.-F. Song, M. Troyer, and A. A. Soluyanov, Comput. Phys. Commun. **224**, 405 (2018).

[55] J.-L. Lu, W. Luo, X.-Y. Li, S.-Q. Yang, J.-X. Cao, X.-G. Gong, and H.-J. Xiang, Chin. Phys. Lett. **34**, 057302 (2017).

[56] A. M. Ganose, A. Searle, A. Jain, and S. M. Griffin, J. Open Source Softw. **6**, 3089 (2021).

[57] P. Giannozzi, S. Baroni, N. Bonini, M. Calandra, R. Car, C. Cavazzoni, and Ceresoli, J. Phys.: Condens. Matter **21**, 395502 (2009).

[58] N. Troullier and J. L. Martins, Phys. Rev. B **43**, 1993 (1991).

[59] N. Marzari, D. Vanderbilt, A. De Vita, and M. C. Payne, Phys. Rev. Lett. **82**, 3296 (1999).

[60] P. B. Allen and R. Dynes, Phys. Rev. B **12**, 905 (1975).

[61] M. Nakhaee, S. A. Ketabi, and F. M. Peeters, Comput. Phys. Commun. **254**, 107379 (2020).

[62] H. Zhao, H. Li, B. R. Ortiz, S. M. Teicher, T. Park, M. Ye, Z. Wang, L. Balents, S. D. Wilson, and I. Zeljkovic, Nature (London) **599**, 216 (2021).

[63] X. Wu, T. Schwemmer, T. Müller, A. Consiglio, G. Sangiovanni, D. Di Sante, Y. Iqbal, W. Hanke, A. P. Schnyder, M. M. Denner *et al.*, Phys. Rev. Lett. **127**, 177001 (2021).

[64] L. M. Schoop, L. S. Xie, R. Chen, Q. D. Gibson, S. H. Lapidus, I. Kimchi, M. Hirschberger, N. Haldolaarachchige, M. N. Ali, C. A. Belvin *et al.*, Phys. Rev. B **91**, 214517 (2015).

[65] H. Tang and S. Ismail-Beigi, Phys. Rev. Lett. **99**, 115501 (2007).
[66] C. Sevik, J. Bekaert, M. Petrov, and M. V. Milošević, Phys. Rev. Mater. **6**, 024803 (2022).
[67] L.-M. Yang, V. Bačić, I. A. Popov, A. I. Boldyrev, T. Heine, T. Frauenheim, and E. Ganz, J. Am. Chem. Soc. **137**, 2757 (2015).
[68] B. Feng, B. Fu, S. Kasamatsu, S. Ito, P. Cheng, C.-C. Liu, Y. Feng, S. Wu, S. K. Mahatha, P. Sheverdyaeva *et al.*, Nat. Commun. **8**, 1007 (2017).
[69] Y. Jing and T. Heine, J. Am. Chem. Soc. **141**, 743 (2019).
[70] G. Galeotti, F. De Marchi, E. Hamzehpoor, O. MacLean, M. Rajeswara Rao, Y. Chen, L. V. Besteiro, D. Dettmann, L. Ferrari, F. Frezza *et al.*, Nat. Mater. **19**, 874 (2020).
[71] B. Feng, J. Zhang, Q. Zhong, W. Li, S. Li, H. Li, P. Cheng, S. Meng, L. Chen, and K. Wu, Nat. Chem. **8**, 563 (2016).
[72] Y. Kato, N. Shiraishi, N. Tsuchimine, S. Kobayashi, and M. Yoshimoto, J. Cryst. Growth **312**, 378 (2010).